IOPscience iopscience.iop.org

Home Search Collections Journals About Contact us My IOPscience

Phases and phase transitions of hexagonal cobalt oxide films on Ir(100)-(1 × 1)

This article has been downloaded from IOPscience. Please scroll down to see the full text article.

2009 J. Phys.: Condens. Matter 21 185003

(http://iopscience.iop.org/0953-8984/21/18/185003)

View the table of contents for this issue, or go to the journal homepage for more

Download details:
IP Address: 129.252.86.83
The article was downloaded on 29/05/2010 at 19:30

Please note that terms and conditions apply.

J. Phys.: Condens. Matter **21** (2009) 185003 (10pp) doi:10.1088/0953-8984/21/18/185003

Phases and phase transitions of hexagonal cobalt oxide films on Ir(100)-(1 × 1)

K Biedermann, M Gubo, L Hammer and K Heinz

Lehrstuhl für Festkörperphysik, Universität Erlangen-Nürnberg, Staudtstraße 7, D-91058 Erlangen, Germany

E-mail: klaus.heinz@physik.uni-erlangen.de

Received 22 December 2008, in final form 2 February 2009
Published 11 March 2009
Online at stacks.iop.org/JPhysCM/21/185003

Abstract
Cobalt oxides on the unreconstructed Ir(100) surface were prepared by reactive deposition of Co established by simultaneous oxygen flux at about 50 °C and subsequent annealing. The films were investigated by low-energy electron diffraction (LEED), scanning tunnelling microscopy (STM) and thermal desorption spectroscopy (TDS). We show that in spite of the quadratic unit mesh of the substrate, oxide films of (111) orientation develop. As long as oxygen-rich conditions are maintained they are of spinel-type $Co_3O_4(111)$. They are non-pseudomorphic and transform to rocksalt-type CoO(111) when oxygen loss is induced by annealing at elevated temperatures. Thin films of CoO(111) are commensurate, and so, in order to realize that, they exhibit a slightly distorted unit cell when below a thickness equivalent to about seven cobalt monolayers. With increasing film thickness the uniaxial strain accompanied by the commensurability is gradually relieved by the insertion of dislocations so that eventually the film assumes ideal hexagonality. All CoO(111)-type surfaces are reconstructed at low sample temperatures equivalent to a $(\sqrt{3} \times \sqrt{3})R30°$ superstructure. They reversibly transform into a (1 × 1) phase at about 50 °C.

(Some figures in this article are in colour only in the electronic version)

1. Introduction

Ultrathin films of transition metal oxides have been the subject of intense research for many years due to their technical importance and often unusual physical properties. In many cases it appears that different phases of oxides coexist with each other on the surface. This is different for the present paper in which we show that all oxides of cobalt developing by epitaxial growth on Ir(100) can be prepared as single phases. In particular we present their structurally and morphologically rich scenario dependent on the preparation procedure and temperature as well as on the stoichiometry and film thickness. The differences are with respect to the morphology of the films, their bulk structure and their surface periodicity. We also describe reversible and irreversible transitions between some of the phases. The choice of the iridium substrate and of the transition metal Co was motivated on the one hand by the fact that the lattice parameters of the different native cobalt oxides are considerably different from those of the Ir substrate, so that (100)-oriented oxides—to be expected because of symmetry—should be non-pseudomorphic. On the other hand motivation came from our experience of preparing nanostructures by deposition of transition metals as Fe, Co and Ni on Ir(100) [1–3]. For reasons of simplicity we don't use the stable phase of the Ir(100) surface, i.e. the quasihexagonally reconstructed Ir(100)-(5 × 1) phase [4, 5], but the structurally much simpler (unreconstructed) metastable phase, Ir(100)-(1 × 1). As methods of investigation we apply scanning tunnelling microscopy (STM), quantitative low-energy electron diffraction (LEED) and thermal desorption spectroscopy (TDS). Some of the oxides have already been described as single phases either qualitatively [6] or by quantitative structure determinations [7, 8]. The latter allow the crystallographic identification of the phases within the preparational phase diagram, which will be presented as new information.

In section 2 we describe experimental details and in particular the way in which the oxide films were prepared. In section 3 we provide the reader with the stable bulk phases of cobalt oxide as these will most likely be realized in the bulk of the films. Subsequently, in section 4, we give a survey of the phases developing as a function of film thickness and

 © 2009 IOP Publishing Ltd Printed in the UK

preparation procedure. Thereby it will become evident that—in spite of the square symmetry of the substrate—all films prepared in the way to be described are of (111) orientation. Section 5 addresses the morphology, order and crystallography of the different phases which can be grouped into spinel-type Co_3O_4 (111) and rocksalt-type CoO(111). Finally, the results are discussed in section 6.

2. Experimental details

A two-stage ultra-high vacuum (UHV) apparatus was used to perform the experiments. One of the vessels hosts homemade four-grid LEED optics as well as a quadrupole mass spectrometer for TDS. The second vessel is supplied with a commercial beetle-type STM (RHK Instruments, Inc.) and there is easy transfer between the two parts. The Ir(100)-(1 × 1) substrate was prepared by lifting the hexagonal reconstruction of the stable Ir(100)-(5 × 1) phase by oxygen adsorption. In a second step, hydrogen is offered to this adsorbate, removing oxygen from the surface and leaving a well ordered clean (1 × 1) surface behind [9–11]. Though this is thermodynamically metastable when clean, it becomes stable when covered with an adsorbate, in particular with the films considered in the present paper.

Cobalt oxide films were prepared by deposition of Co under oxygen-rich conditions, i.e. under simultaneous O_2 flux. An electron-beam evaporator supplied with highly purified Co was used for metal deposition. It was operated at a deposition rate of about 1 monolayer (ML) min^{-1} and a sample temperature of about 50 °C (1 ML Co corresponds to a coverage of 1.36×10^{15} cm^{-2} on Ir(100)-(1 × 1)). A doser positioned in front of the sample was used to simultaneously establish a high oxygen flux according to an increased local oxygen pressure near the sample, which is estimated to be at least 10^{-6} mbar. Films deposited at a lower substrate temperature (down to that of liquid nitrogen) were of similar morphology whilst deposition temperatures above about 100 °C instantaneously led to a three-dimensional (3D) growth mode as identified by LEED patterns typical for facetted surfaces. Furthermore, it should be noted that preparation under less oxygen-rich conditions produces films of different (i.e. non-hexagonal) symmetry; this will be addressed in a forthcoming paper.

The films resulting from the procedure described were of poor order initially. Yet subsequent annealing at 250 °C for 2 min with the oxygen flux maintained improved the order substantially. The thickness of the films—given in terms of the number of Co monolayers deposited (monolayer equivalents, MLE)—is in the range of roughly N_{Co} = 2–50 MLE. Eventually, in order to allow for additional ordering processes, the films were post-annealed in UHV whereby the temperatures were chosen to reach LEED patterns with the sharpest spots and lowest background possible.

STM images were taken for the sample at room temperature; for films turning out to be of CoO stoichiometry atomic resolution could be achieved with (positive) tip voltages in the mV range in spite of the to-be-expected insulating character of the oxide. LEED patterns and intensity versus energy spectra, $I(E)$, were recorded for use as fingerprints to characterize the development of the oxide (and also as input for the structural analysis of the fully developed oxide in a separate work). They were measured using a 12-bit digital charge-coupled-device (CCD) camera viewing the LEED screen from outside the UHV. The patterns were stored on a computer hard disk in energy steps of 0.5 eV and the $I(E)$ spectra result from off-line evaluation of the video signal under computer control with automatic background subtraction involved [12]. When necessary, different $I(E)$ spectra are compared quantitatively by use of the Pendry reliability factor R [13]. The TDS measurements were performed by applying a linear increase of the sample temperature with time and simultaneous measurement of the signal of desorbing oxygen in the quadrupole mass spectrometer. The latter was provided with a cap with a small opening close to the surface, so that oxygen desorbing exclusively from the sample entered the spectrometer.

3. Bulk phases of cobalt oxide

Bulk cobalt oxide crystals appear in two stable crystallographic structures, the rocksalt-type CoO and the normal-spinel-type Co_3O_4. They are displayed in perspective and top view in figure 1 with (111) orientation chosen for the layers that appear because this meets, as it turns out, the film orientation realized in experiment. In both cases the oxygen layers are basically hexagonally close packed and arranged in face centred cubic (fcc) stacking, alternating with layers made up of cobalt. Whilst the oxygen layers are flat in CoO they are vertically buckled by an amplitude $b = 0.121$ Å in Co_3O_4 as calculated from crystallographic data given in [14]. This is because in CoO the cobalt layers are also hexagonally close packed with the Co^{2+} ions residing exclusively in octahedral sites, whilst in Co_3O_4 the cobalt layers alternating with oxygen layers are different. Every second one consists of Co^{3+} ions, again exclusively in octahedral sites with, however, only three out of four such sites occupied equivalent to a (2 × 2) supercell with respect to the hexagonal cell of the oxygen layer as indicated in figure 1(b). Accordingly, the ionic charge is $+9e$ per unit cell. The second type of cobalt layer has the same ion density as the first but consists of three sublayers with cobalt ions in different coordination. The centre sublayer is made up of Co^{3+} ions in octahedral sites whilst the other two sublayers consist of Co^{2+} ions in tetrahedral sites. So the total charge of the three sublayers is $+7e$ per unit cell, whilst that of the oxygen layers is $-8e$ each.

The cubic lattice parameters of rocksalt-type CoO and spinel-type Co_3O_4 are $a_R = 4.260$ Å and $a_S = 8.084$ Å, respectively. Accordingly, the corresponding lengths of the vertical repeat unit of layers are $d_R = a_R\sqrt{3}/3 = 2.460$ Å and $d_S = a_S\sqrt{3}/3 = 4.667$ Å as in the inset in figure 1. The in-plane lattice parameters of the layers are $a_{R,p} = a_R/\sqrt{2} = 3.012$ Å and $a_{S,p} = a_S/\sqrt{2} = 5.716$ Å with the corresponding unit-mesh areas $A_R = a_R^2\sqrt{3}/4 = 7.858$ Å^2 and $A_S = a_S^2\sqrt{3}/4 = 28.30$ Å^2. We also recall the lattice parameter of Ir(100) which is $a_{Ir} = 3.840$ Å with $a_{Ir,p} = a_{Ir}/\sqrt{2} = 2.715$ Å holding for the quadratic in-plane unit cell.

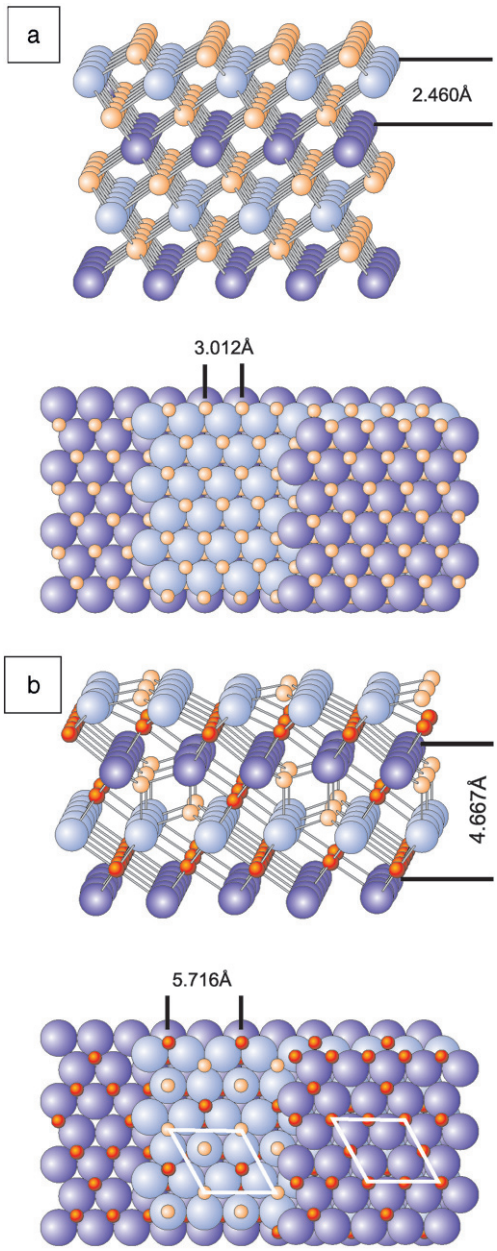

Figure 1. Stable bulk phases of cobalt oxide in perspective and top view of (a) rocksalt-type CoO and (b) spinel-type Co_3O_4, both in (111) orientation. Oxygen (cobalt) ions are represented by large (small) balls. Co^{2+} (Co^{3+}) ions appear by light (dark) red shading of the balls.

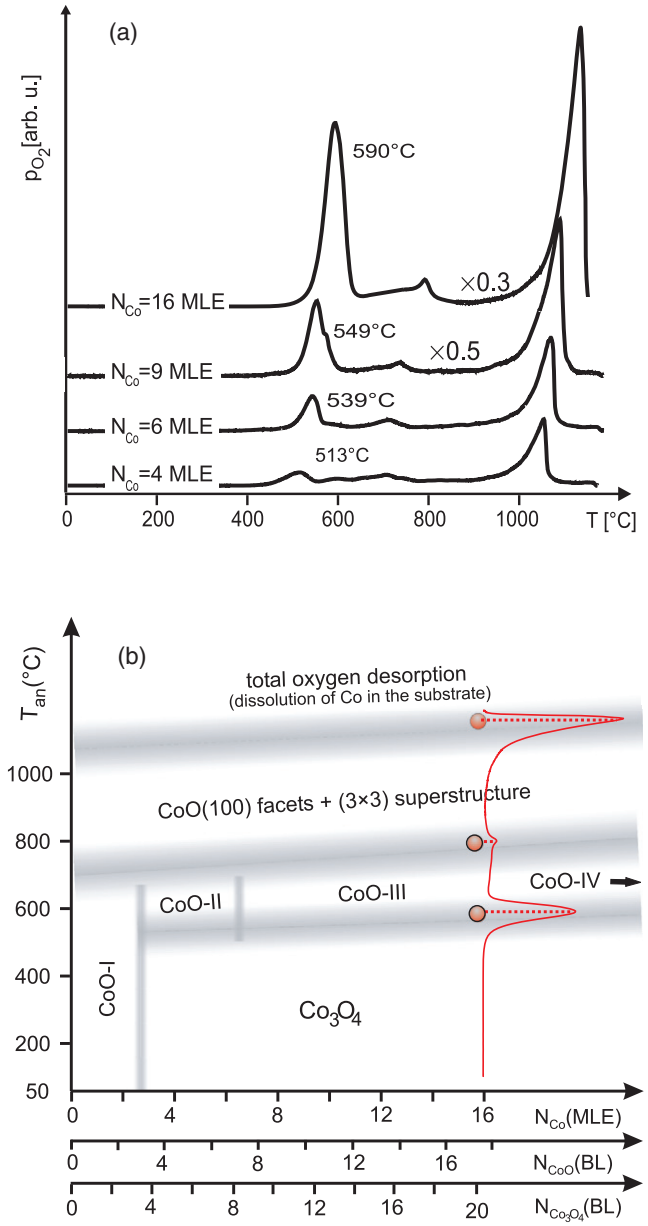

Figure 2. (a) Thermal desorption spectra of oxygen from films of different thicknesses prepared under oxygen-rich conditions (note that the high temperature peak of the 16 MLE curve is not fully developed). (b) Preparation diagram for oxygen-rich oxide preparation as function of the number N_{Co} of cobalt monolayer equivalents (MLE) oxidized and the temperature T_{an} at which the resulting film was annealed in UHV. A TD spectrum (for $N_{Co} = 16$ as an example) is shown in the insert to demonstrate how the horizontal phase boundaries are determined. The additional abscissa give the film thickness in terms of the numbers of oxide bilayers (BL) for CoO(111) and Co_3O_4 (111) whereby $N_{Co_3O_4} = (1/2\sqrt{3})(a_S/a_{Ir})^2 N_{Co} \approx 1.28 N_{Co}$. The relation for ideally hexagonal CoO is $N_{CoO} = (\sqrt{3}/2)(a_R/a_{Ir})^2 N_{Co} \approx 1.07 N_{Co}$ and for distorted CoO it is $N_{CoO} = \frac{10}{9} N_{Co}$.

4. Survey of the different oxide-film phases

Annealing of the oxide films at elevated temperatures leads to a loss of oxygen which was monitored by TDS. This is demonstrated in figure 2(a) for oxides of different thicknesses starting in each case with a film prepared under oxygen-rich conditions. A first considerable loss of oxygen occurs between 500 and 600 °C whereby the desorption starts earlier the thinner the film. A second and comparably small desorption peak develops between 700 and 800 °C, indicative of only a small loss of oxygen. It is followed by another strong peak at temperatures above 1000 °C at which—as it is the last peak in the spectrum—all oxygen still present desorbs, i.e. the oxide fully decomposes. No species other than O_2 desorbing from the surface were found. Therefore, without going into the desorption kinetics involved in the spectra, we can estimate the relative amount of oxygen desorbed during development

of the first desorption peak. Comparison of the area below it with the total area of a spectrum tells us that about a quarter of oxygen is lost by the film. This is indicative of the oxygen rich oxide phase being Co_3O_4 and its transformation to CoO when annealed at a temperature above the first desorption peak, which in fact has been confirmed by quantitative LEED [7, 8].

By using the desorption peak temperatures as function of film thickness (measured by the number N_{Co} of Co monolayers oxidized) the corresponding horizontal phase boundaries can be drawn in the preparation diagram T_{an}–N_{Co}. This diagram is displayed in figure 2(b) whereby the desorption spectrum for $N_{Co} = 16$ is inserted as an example (the points of the phase boundaries determined from it are indicated by small spheres). In the low temperature regime spinel-type Co_3O_4 develops except for the region below $N_{Co} \approx 3$ MLE in which a certain phase of CoO prevails (CoO-I). Other phases of this stoichiometry develop above the lowest horizontal phase boundary and are denoted as CoO-II, CoO-III and CoO-IV.

At annealing temperatures corresponding to the small peak in the TD spectra there is little loss of oxygen. So, the 1:1 stoichiometry largely prevails, but there is substantial reordering in the film leading to CoO(100) facets with a (3×3) superstructure (relative to the Ir(100) substrate) superimposed. At even higher annealing temperatures exceeding 1000 °C the oxides decompose completely. Oxygen then desorbs from the surface whilst cobalt dissolves into the substrate's bulk.

The vertical phase boundaries can be drawn from the information provided by LEED patterns and STM images as a function of film thickness in the temperature ranges between the horizontal phase boundaries. Figure 3 summarizes this information. Surprisingly, in view of the square symmetry of the iridium substrate, all films appear in (111) orientation, i.e. with a hexagonal in-plane unit mesh which, however, can be slightly distorted. Below $N_{Co} \approx 3$ MLE there is (in terms of the substrate's unit cell) a $c(10 \times 2)$ superstructure with two orthogonal domains as displayed in figure 3(a). The STM image for one domain is given in panel (b) from which it is apparent that the local structure is hexagonal (or at least near hexagonal). The corresponding reciprocal unit cell is given by the full line in panel (a), and the cell of the square substrate by the dotted line. By multiple (at least double) diffraction between substrate and film diffraction spots of the $c(10 \times 2)$ superstructure are created whose primitive unit meshes in reciprocal and real space for one domain are given by the dashed lines in panels (a) and (b), respectively. As also evident from the STM image, the film surface is considerably buckled which is caused by the accommodation of hexagonal layers on a quadratic substrate as has been quantitatively determined in [6]. Because of the detailed description there we do not address the $c(10 \times 2)$ phase further in the present paper.

For thicknesses beyond the equivalent of $N_{Co} \approx 3$ MLE the diffraction contributions from the iridium substrate gradually disappear as for both CoO(111) and Co_3O_4 (111) the thickness ($N_{CoO}d_R$ or $N_{Co_3O_4}d_S/2$, respectively) becomes larger than about 7 Å and so exceeds the electron penetration length (note that the electrons have to travel to the interface and back to the surface). In the regime of low annealing temperatures, i.e. without any loss of oxygen by annealing,

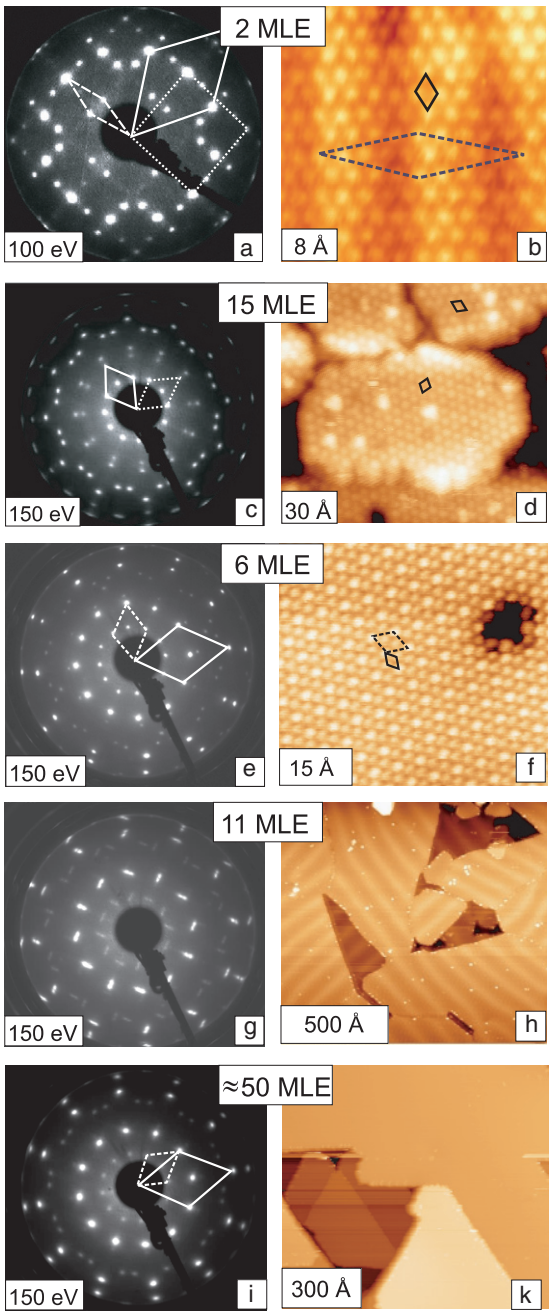

Figure 3. LEED patterns and STM images for films of (a, b) CoO-I, (c, d) Co_3O_4, (e, f) CoO-II, (g, h) CoO-III and (i, k) CoO-IV at film thicknesses as indicated. In patterns (c) and (d) the unit cells of two orthogonal domains are indicated. Patterns (e) and (f) contain the (1×1) cell (full line) and the $(\sqrt{3} \times \sqrt{3})R30°$ cell (broken line) for one of two orthogonal domains. Tunnelling conditions for the STM images displayed are: (b) 0.15 V, 2.0 nA; (d) −2.78 V, 0.67 nA; (f) −0.130 V, 8.82 nA; (h) 3.55 V, 4.75 nA; (k) 2.88 V, 0.47 nA.

Co_3O_4(111) develops independent of film thickness. The corresponding LEED pattern (figure 3(c)) is ideally hexagonal with again two orthogonal domains present due to the four-fold symmetry of the substrate (the two unit cells are indicated). The corresponding surface patches appear rather flat, i.e. there is no apparent buckling in the STM image (panel (d)). When this phase is annealed between 500 and 600 °C the induced loss

of oxygen leads to CoO, whereby, however, different phases of this stoichiometry develop dependent on film thickness. With respect to the unit cell of CoO(111) they all exhibit a $(\sqrt{3} \times \sqrt{3})$R30° superstructure. For $N_{Co} \leqslant 7$ MLE the cell is distorted (phase CoO-II), i.e. it is only near hexagonal (figures 3(e) and (f)). With increasing film thickness it becomes (almost) ideally hexagonal (phase CoO-III) but is superimposed by a long-range corrugation (figures 3(g) and (h)). The latter disappears with further increasing thickness of the oxide (phase CoO-IV, figures 3(i) and (k)). When the second horizontal phase boundary is crossed the surface develops facets as can be judged by the way LEED spots move when the energy is varied. The evaluation of their traces indicates that the facets are of {100} orientation. Additionally, there is a superimposed (3 × 3) superstructure (relative to Ir(100)). Its $I(E)$ spectra are identical to those of a single monolayer (3 × 3) superstructure on Ir(100) formed in oxygen-poor preparation conditions. Its structure as determined by quantitative LEED will be published in a separate paper [15].

5. Crystallography and morphology of the different phases

5.1. Co_3O_4(111) films

As given in the preparation diagram, the Co_3O_4 phase develops for annealing temperatures that are not too elevated and above $N_{Co} \approx 3$ MLE. The corresponding films are flat and exhibit LEED patterns and STM images typical for a hexagonal arrangement of the ionic species. In the range investigated, i.e. $N_{Co} \approx 3$–50 MLE (that is $N_{Co_3O_4} \approx 4$–64 BL), the LEED spots are sharp and their intensity spectra are almost identical (mutual Pendry R-factors $R \leqslant 0.1$), i.e. the Co_3O_4(111) phases in this range are crystallographically equivalent.

From STM images taken at a smaller scale than that displayed in figure 3(d) a unit cell length of 5.7 Å is taken. Careful evaluation of the LEED pattern given in figure 3(c) yields an even more precise value of 5.72 Å. This is in quantitative agreement with the native in-plane lattice parameter of bulk spinel-type Co_3O_4(111), i.e. $a_{S,p} = 5.716$ Å. As a consequence, the films are laterally fully relaxed and thus incommensurate, only the orientation of the hexagon is fixed by the substrate, i.e. one of the hexagonal unit-mesh vectors is along the [011] or [0$\bar{1}$1] vectors of the substrate (orientational epitaxy). In similar agreement with the bulk spinel structure are the step heights retrieved by STM. They are largely dominated by values in the range 4.6–4.7 Å, reproducing the length of the vertical repeat unit in Co_3O_4(111), which is $d_S = 4.667$ Å. So, the bulk of the film apparently is that of native Co_3O_4 which has in fact been confirmed by a recent quantitative LEED intensity analysis by our group [7]. The latter shows that the film is terminated as displayed in the upper panel of figure 1(b), i.e. by a sublayer of cobalt ions which in the bulk were tetrahedrally coordinated Co^{2+} ions. There are drastic layer relaxations at and near the surface which has been interpreted to be due to a substantial change of the ionicity of the ions involved [7].

STM images, in particular atomically resolved ones, could be recorded for tunnelling voltages in the range 2–3 V or −(2–3) V. Tunnelling with a voltage in the range $-2 \cdots +2$ V almost never produced an image, indicative for an energy gap around the Fermi energy of about 4 eV. This value is larger than those reported for other (and differently prepared) thin films of Co_3O_4, i.e. 1.3–1.6 eV for the indirect band gap and 2.0–2.2 eV for the direct band gap dependent on film preparation [16–19]. The latter values are deduced from optical measurements probing the bulk of the films, whilst the STM tip current depends on the surface electron density which might be rather different from that of the film's bulk due to the substantial surface relaxation.

5.2. CoO(111) films

As demonstrated in figure 3 the LEED patterns developing with the annealing of Co_3O_4(111) films just beyond the first desorption peak (crossing the lowest horizontal phase boundary in figure 2(b)) all exhibit a $(\sqrt{3} \times \sqrt{3})$R30° superstructure relative to the unit cell of bulk terminated CoO(111) which, of course, complicates a quantitative structure determination of the films. Yet there is a (reversible) transition towards a (1 × 1) pattern when the sample temperature is increased beyond about $T_c \approx 50$°C. We address this transition first and subsequently concentrate on the shape and size of the surface unit cells of the CoO-II, CoO-III and CoO-IV phases. Eventually, we resume their crystallographic structure which has been determined by quantitative LEED in separate work [8, 20].

5.2.1. Phase transition $(\sqrt{3} \times \sqrt{3})R30° \leftrightarrow (1 \times 1)$. This transition is illustrated in figure 4 which in the upper panels displays the LEED patterns below and above T_c. Evidently the superstructure spots have disappeared above T_c. In order to follow the temperature driven transition we recorded the temperature dependence of the intensity of a superstructure and integer order spot. Figure 4(c) displays the result: the intensities are corrected for thermal diffuse scattering by dividing through the Debye–Waller factor at each temperature (the effective Debye temperature was determined well below T_c). It appears that the superstructure weakens continuously with approaching T_c whilst the integer order spot intensity remains approximately constant. The latter fact can be due to the circumstance that the fractional order spots are rather weak compared to integer order spots ($I_{frac} \approx 0.06 I_{int}$ on energy average) indicative of only small atomic displacements off the positions in the corresponding (1 × 1) phase. As a consequence, the integer order intensities are not considerably modified by the disappearance of the superstructure in the structural transition. At present we cannot judge whether this transition is of order–order or order–disorder type (in the latter only long-range order of the superstructure would disappear so that integer order spot intensities would remain unaffected as LEED intensities are formed locally due to the finite electron attenuation length [12, 21]).

The inspection of the spectral features of the integer order beams before and after the structural transition as displayed in

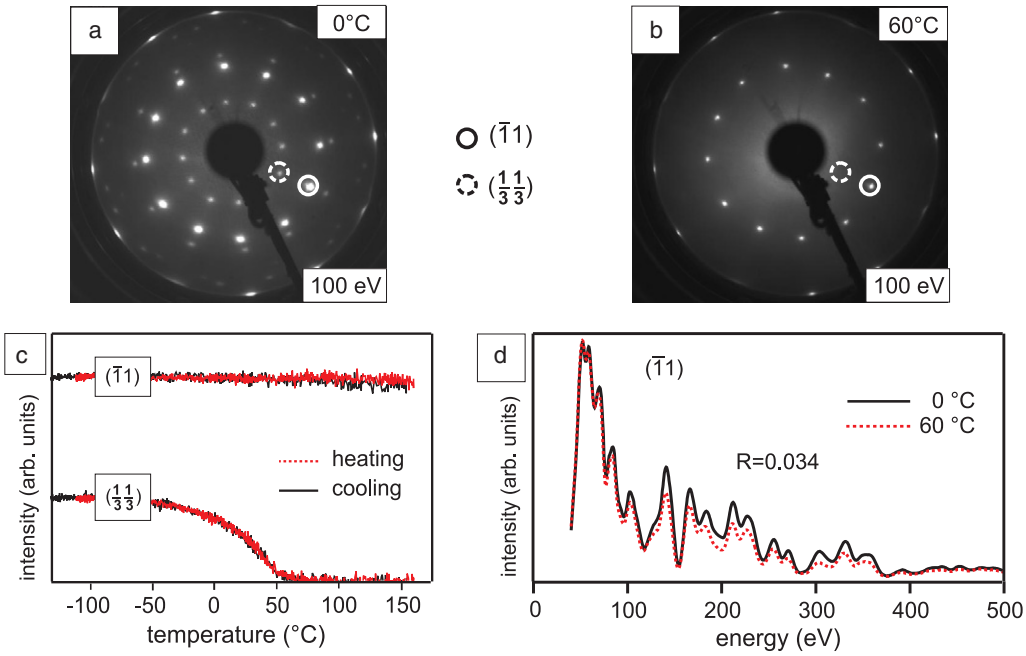

Figure 4. LEED patterns of CoO(111) for $N_{\mathrm{Co}} = 6$ MLE (a) below and (b) above $T_c \approx 50\,°\mathrm{C}$. Panel (c) displays the intensities of the $(\bar{1}1)$ and the $(\frac{1}{3}\frac{1}{3})$ spots of two orthogonal domains at 100 eV as a function of temperature corrected for thermal diffuse scattering (the spots are encircled in panels (a) and (b)). In diagram (d) the spectra of the $(\bar{1}1)$ spot of the two phases are compared.

figure 4(d) (here uncorrected for thermal diffuse scattering but normalized with respect to each other at the maximum peak) does not allow us to decide between order–order and order–disorder transition either. As is obvious by visual inspection, as well being as mirrored by the very low R-factor ($R = 0.034$ for the $(\bar{1}1)$ beam as an example), the spectra are almost identical. Yet this can again be due to the low intensity of superstructure spots or to the loss of only long-range order of the superstructure. In any case, however, it proves that there are only small differences between both phases with respect to atomic positions.

5.2.2. Symmetry, lattice parameters and film morphology. At first glance the LEED patterns of the different CoO phases (figures 3(e), (g) and (i)) appear to be all of the same hexagonal symmetry (though the pattern of CoO-III given in panel (g) differs by split spots). Yet comparison of the intensities of beams which, for ideal hexagonality (including the two types of fcc stacking) would be symmetrically equivalent at normal electron incidence, shows that the hexagonal symmetry is clearly broken for the CoO-II phase. This is demonstrated by figure 5. Panel (a) repeats the LEED pattern of this phase (with spots of the two orthogonal domains indicated by different symbols) and panel (b) exhibits the spots of one domain only. In diagram (c) the spectra of two such equivalent beams (framed in panel (b)) are displayed. There are significant differences expressed by a mutual Pendry R-factor $R = 0.391$. A close inspection of the shape of the surface unit-mesh cell of phase CoO-II also reveals that it is distorted off the ideal hexagonal cell in very much the same way as that of phase CoO-I: compared to the ideal unit cell of CoO(111) with $a_{\mathrm{R},p} = 3.012$ Å the unit cell vectors are about 3.02 and 3.11 Å long with two of the 60° angles distorted to about 61°. In this sense the CoO-II phase is a pseudomorphic continuation of the CoO-I phase.

The LEED pattern of CoO-III (figure 3(g)) differs from that of CoO-II in two ways. First, as is clearly visible the diffraction spots are split or at least become very elongated. The splitting is reproduced in the schematic diffraction pattern displayed in figure 6(a) with the splitting direction indicated by the broken line. Second, the distortion of the hexagonal unit cell has largely disappeared. The latter fact can be proved again by comparison of intensity spectra of beams which, at normal incidence of the primary beam, are symmetrically equivalent for ideal hexagonal symmetry. These are, for example, the spots (more precisely, split spot pairs) framed in figure 6(a). Their spectra, which are displayed in panel (b), are much more similar than for thinner films (see figure 5(c)) with a mutual Pendry R-factor as low as $R = 0.111$. Nevertheless, this value is still high enough to indicate that some residual distortion of the film off ideal hexagonality has remained. A value of $R = 0.111$ in our case cannot be caused by experimental insufficiencies (for example sample misalignment) as is proved by comparison of the (10) and $(\bar{1}1)$ spots which are fully degenerate due to grain twinning and for which the R-factor is as low as $R = 0.007$.

The spot splitting is connected to a long-periodic buckling of the film which leads to the appearance of stripes in the STM image (figure 3(h)). In LEED such a long-periodic buckling should lead to superstructure spots with the diffraction angle between these spots varying with energy. Yet this only applies when the coherence length of the LEED optics used is large compared to the buckling period. In the present case we use ordinary optics with a coherence length of the order of 100 Å.

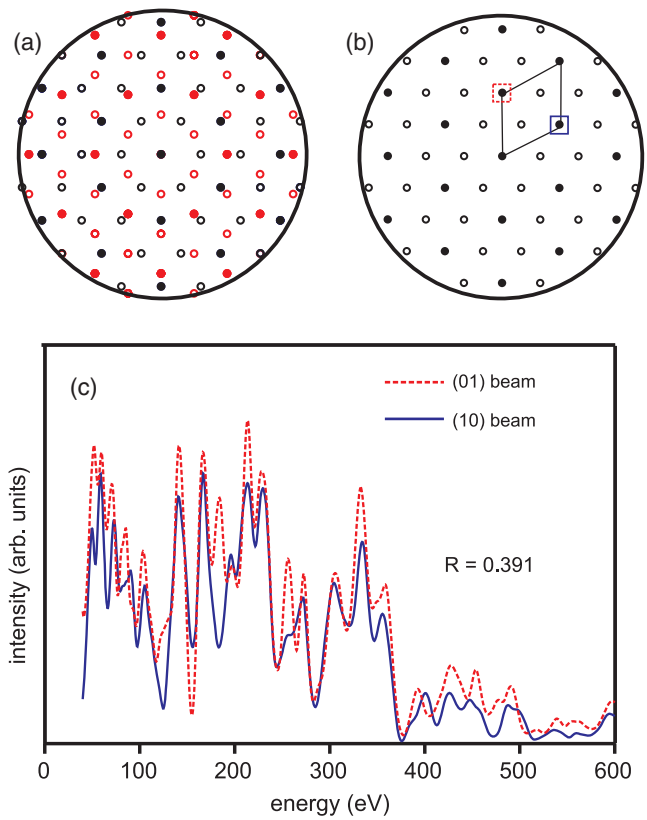

Figure 5. Schematic representation of the $(\sqrt{3} \times \sqrt{3})$R30° LEED pattern given in figure 3(e) for (a) both orthogonal domains and (b) for only one domain. Panel (c) displays the intensity spectra recorded for normal incidence of the primary electrons for two beams (framed in panel (b)) which would be degenerate for ideally hexagonal layers.

Quantitative evaluation of the STM image by a height profile as given in figure 6(d) and approximated by a periodic zig-zag line shows that the (average) period $L_b = 577/6$ Å ≈ 96 Å is of the same order, so no superstructure spots should occur. Instead, the surface morphology must be viewed as an array of quasi-microfacets whose tilt angle ϑ with respect to the substrate plane alternates in sign. With a buckling amplitude of $h = 0.50$ Å (as taken from the STM profile) the tilt angle turns out to be $\vartheta = \pm\arctan(2h/L_b) \approx \pm 0.6°$. This causes a spot splitting (rather than superstructure spots with energy dependent angular spacings) by an angle of 4ϑ independent of energy as observed in experiments. The split angle 2° determined from the LEED pattern agrees within the error limits with 4ϑ.

A closer inspection of the STM appearance of the surface protruding stripes as a function of film thickness reveals the following. In comparably thin films they are rather narrow and irregularly spaced (not shown) but gain in width and regularity with increasing thickness. We interpret these lines as the displacement field of edge dislocations which run along the $[0\bar{1}1]$ direction and are buried to a certain depth within the film. The occurrence of such misfit dislocations has to be expected at a critical film thickness in order to relieve the film stress which would grow linearly with thickness. When they start to form at comparably small film thickness the dislocation line is right below the surface so that the distortion is laterally rather local and considerable vertical atomic displacements can result (STM profiles of 7 MLE film reveal vertical displacements of up to 0.8 Å). With further increasing film thickness the dislocation lines become more distant from the film surface so that the displacement fields get smoother. Eventually they overlap with each other forming an almost periodically modulated, i.e. microfacetted, surface as displayed in figure 3(h) for a 11 MLE film. Accordingly, the corrugation amplitude of the film surface decreases with film thickness (it is, for example, only 0.3 Å for a 14 MLE film) until it finally vanishes completely. The development of misfit dislocations has also been proposed for (100) oriented films of CoO [22] and MgO [23, 24] on the basis of both diffraction experiments and transmission electron microscopy. In both cases split diffraction spots similar to our case were found. For the system MgO/Fe(100) they were quantitatively interpreted by the elastic displacement fields of misfit dislocations [25].

Full relaxation of the CoO-III oxide film would mean that the lengths of the in-plane unit-mesh vectors are that of native CoO(111), i.e. $a_{R,p} = 3.012$ Å. This can be checked with high precision by taking advantage of the fact that the lateral buckling periodicity must be $N_L = L_b/a_{Ir,p}$. Assuming further that now $(N_L + 1)$ oxide rows with spacing $D = \sqrt{3}a_{R,p}/2$ (with $a_{R,p}$ the hexagonal in-plane film unit-mesh length) fit into L_b—since the film was formerly expanded in that direction in order to fit the row spacing—we obtain from $L_b = N_L a_{Ir,p} = (N_L + 1)\sqrt{3}a^{F}_{R,p}/2$ the value $a^{CoO-III}_{R,p} = 2L_b a_{Ir,p}/(\sqrt{3}(L_b + a_{Ir,p})) \approx 3.05$ Å. This is still expanded by 1.2% with respect to the native value of $a^{bulk}_{R,p} = 3.012$ Å. The latter is not fully restored even for a film of thickness as much as 50 MLE (CoO-IV). This can be judged again by the comparison of $I(E)$ spectra of the (10), (01) and $(\bar{1}1)$ spots which would be degenerate in the case of ideal hexagonality. Yet, even for the 50 MLE film the R-factor between (10) and (01) spot intensities is small but significantly larger ($R = 0.031$) than for the intensities of the symmetrically equivalent (10) and $(\bar{1}1)$ spots ($R = 0.003$). This rather slow relaxation of the lateral lattice parameters with increasing film thickness is also in accordance with findings for other oxide films (e.g. [22, 24]).

5.2.3. Crystallography of the CoO films. Both the surface unit-mesh geometry discussed above as well as the step heights retrieved from STM images—which turn out to be about 2.5 or 4.9 Å in accordance with the vertical repeat length of rocksalt CoO (see figure 1(a))—favour that at least the bulk of the CoO films is of rocksalt structure. The final proof for that comes by a quantitative LEED analysis for a CoO(111) film with a thickness equivalent to $N_{Co} \approx 6$ MLE, that is with a distorted hexagonal unit-mesh (CoO-II), which was recently performed for the (1×1) phase at $T > T_c$ [8]. Ideal (1×1) order was assumed. Yet, only by allowing a near surface fault in the bulk-like fcc stacking of layers was a convincing and even excellent theory–experiment fit found ($R = 0.114$). The surface is oxygen terminated and the stacking fault appears by a registry shift of the second layer, i.e. the first cobalt layer. As a consequence the coordination of ions in the top three layers is wurtzite like (in fact wurtzite-type CoO has been

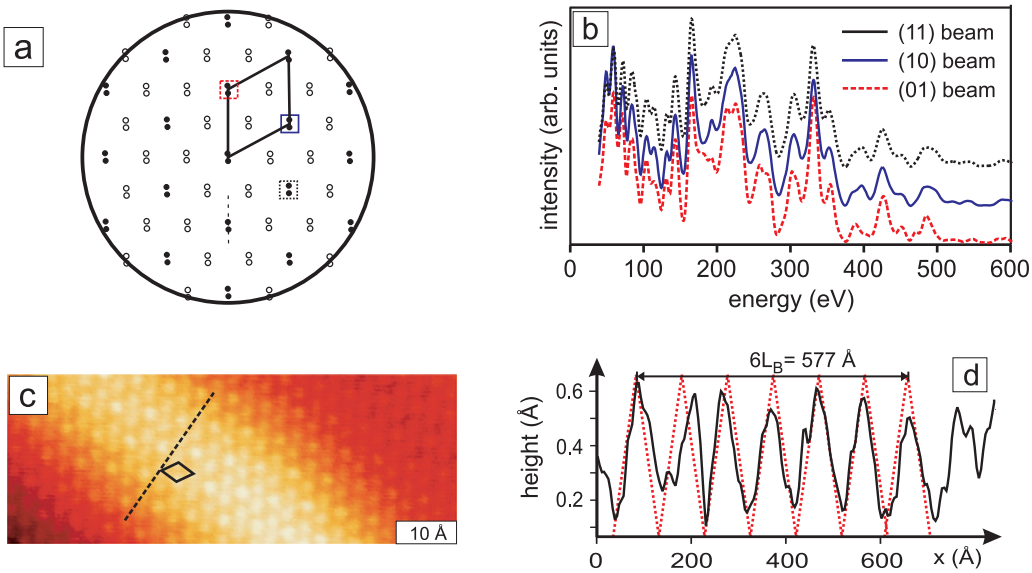

Figure 6. (a) Schematic representation of the LEED pattern for two orthogonal domains of the $(\sqrt{3} \times \sqrt{3})$R30° structure as given in figure 3(g). The splitting directions of spots are indicated and the (1×1) unit cell is inserted. In panel (b) the intensity spectra recorded for normal incidence of the primary electrons are compared for three beams (framed in panel (a)) which are symmetrically equivalent for ideally hexagonal layers. Panel (c) displays an atomically resolved part of the image in figure 3(h). Panel (d) displays a profile through the image figure 3(h) with the broken line indicating a regular arrangement of zig-zag microfacets.

reported to form as small clusters under special preparation conditions [26, 27]). Below that the rocksalt-type fcc stacking is preserved. Due to the thus enforced matching of different stacking sequences there are drastic relaxations of the first few layer spacings off the bulk values. The scenario is not caused by the off-hexagonal distortion of the film, it has also been found for the practically ideally hexagonal film CoO-IV [8].

We point out that the structure of the $(\sqrt{3} \times \sqrt{3})$R30° phase at $T < T_c$ differs from that of the (1×1) phase only by slight atomic displacements as has been found by quantitative LEED structure determination. This was expected from the weak superstructure spots. The full results will be published in a separate work [20].

6. Discussion and conclusion

All oxide films presented and resulting from the special, i.e. oxygen-rich, preparation procedure described are of hexagonal (111) orientation independent of stoichiometry and in spite of the square symmetry of the substrate. This is the more surprising as these Co_3O_4(111) and CoO(111) films are—in contrast to their (100) orientation—polar due to their alternating ionic layers and so, when there is no compensation for the electrostatic dipole moment, should not be stable when growing to substantial thicknesses. For films of rather limited thickness this polarity might not be a serious issue from the energy point of view as the films might be stabilized by interaction with the substrate. Yet we also observe thick films in (111) orientation where interface properties can hardly affect the stability of the whole film. Therefore it is worth remembering that there are numerous ways for polarity compensation (see, e.g., the reviews [28, 29]). They all are based on extra charges created at or near the surface. These can, for example, come by changes of the surface stoichiometry, e.g. due to chemical surface reconstruction, by surface induced changes of the ionicity of surface ions, by occupation of electronic surface states or by adsorption of ionic species (or neutral species which become charged by adsorption). In the present investigation and in the quantitative LEED structure analyses performed independently [7, 8] we have found neither surface reconstructions nor adsorbates. Yet, for Co_3O_4(111) it was determined that the film is terminated by only part of a layer of cobalt ions which in the bulk would have been tetrahedrally coordinated Co^{2+} ions. This leads already to a partial dipole compensation. Additionally there are drastic layer relaxations at and near the surface [7] which can be caused by a substantial change of the ionicity of the ions involved, so that the film may even be fully compensated with respect to polarity. For the CoO(111) films the structure analysis [8] found an oxygen terminated wurtzite-type surface slab with again drastic bond length changes near the surface (equivalent to substantial layer relaxations). This is indicative of a drastic change in the occupation of electronic states at the surface which may account for polarity compensation. Further, the surface appears to be metallic as the STM produces atomically resolved images at bias voltages in the mV range. Yet we cannot decide whether this metallic character of the surface is due to the wurtzite-type stacking at the surface or related to the lattice distortion caused by this. Recent first principles calculations for wurtzite-type CoO contradict each other with respect to the metallic character of the surface [27, 30].

As enforced by the oxygen-rich initial preparation procedure—deposition of Co under simultaneous exposure to oxygen and some further annealing in oxygen—spinel-type Co_3O_4(a_S = 8.084 Å) develops. Its (111) orientation is

surprising in view of the possibility that (100) orientation could be realized by occupation of every second hollow site of the Ir substrate (a_{Ir} = 3.840 Å) with only a 5% misfit involved. Yet seemingly the corresponding strain costs too much energy compared to the (111) orientation in which the film growth is incommensurate and assumes its native lattice parameter. Possibly, the (111) oriented surface of a polarity compensated film is energetically more favourable than a (100) oriented one, as has been shown for rocksalt-type MgO and NiO [31]. The film's matching to the substrate at the interface might contribute to the stabilization of the (111) orientation. Here, a row-on-row matching is enabled whilst a (100) oriented film would need to form a practically incommensurate interface due to the large (about 10%) mismatch to the substrate (a_R = 4.260 Å versus a_{Ir} = 3.840 Å). Yet it can also be caused by the fact that our CoO(111) films result from annealing of already (111) oriented Co_3O_4 films by oxygen desorption from the oxide so that the (111) orientation is preserved in this process. The conversion temperature increases to some extent with the film thickness obviously due to the restructuring of an increasing amount of material involved and/or to the necessary diffusion of oxygen through a film of increasing thickness. For film thicknesses less than $N_{Co} \approx 7$ MLE the CoO(111) films assume an epitaxial arrangement forming a coincidence lattice with the substrate which can be approximately described as a c(10×2) superstructure. (For film thicknesses larger than about 3 MLE this superstructure does not appear in the LEED pattern because the substrate is hidden by electron attenuation and the induced film corrugation has decreased or even vanished.) Due to the accommodation to the substrate the hexagonal unit-mesh of the films is slightly distorted both with respect to its shape and its unit-mesh vector lengths. This uniaxial distortion gradually disappears with increasing film thickness due to the development of misfit dislocations. Presumably these dislocations are of the same $\frac{1}{2}\langle 011\rangle\{011\}$ type as those unambiguously identified for MgO films [24, 25] since the preferential slip systems are the same for MgO and CoO [32]. Most probably, the dislocation lines are located some layers above the interface, so that—as a consequence—the one-to-one atomic row matching at the interface between film and substrate may still persist.

In contrast to that, no dislocations were found for the Co_3O_4(111) films whose lateral lattice parameter was determined to be bulk like independent of film thickness. This is a clear indication that Co_3O_4 films are incommensurate with the substrate throughout the film including the region at the interface.

All CoO(111) films exhibit a $(\sqrt{3} \times \sqrt{3})$R30° superstructure but with rather weak fractional order spot intensities relative to that of integer order ones. This phase transforms reversibly to a (1 × 1) phase at $T_c \approx 50$ °C whereby the spectra of integer order spots remain almost unmodified. At present it is not fully resolved whether the high temperature phase is strictly ordered, so that there is an order–order transition, or if order is (1 × 1) only on average with features of the $(\sqrt{3} \times \sqrt{3})$R30° structure locally preserved (but lost with respect to long-range order), so that we deal with an order–disorder transition.

In conclusion we have shown that cobalt oxides form on Ir(100) with a variety of different features, yet in any case hexagonally oriented (111) layers parallel to the substrate which is of quadratic order. As long as oxygen-rich preparation conditions are enforced there is non-pseudomorphic growth of Co_3O_4(111) which, due to assuming the native lattice parameter, is unstrained. Annealing of such films leads to the formation of CoO(111). For small film thicknesses they are pseudomorphic, yet at the cost of a distorted hexagonal in-plane unit cell enforcing tensile stress. For thicker CoO(111) films stress release processes gradually lead towards an ideally hexagonal unit-mesh which, however, is still not completely assumed for a film thickness as large as 130 Å.

Acknowledgment

The authors are indebted to Deutsche Forschungsgemeinschaft for financial support.

References

[1] Klein A, Meyer W, Schmidt A, Gumler B, Müller S, Hammer L and Heinz K 2008 *Phys. Rev.* B **78** 045422
[2] Giovanardi C, Klein A, Schmidt A, Hammer L and Heinz K 2008 *Phys. Rev.* B **78** 205416
[3] Heinz K and Hammer L 2009 *Prog. Surf. Sci.* **84** 2
[4] Ignatiev A, Jones A and Rhodin T 1972 *Surf. Sci.* **30** 573
[5] Schmidt A, Meier W, Hammer L and Heinz K 2002 *J. Phys.: Condens. Matter* **14** 12353
[6] Giovanardi C, Hammer L and Heinz K 2006 *Phys. Rev.* B **74** 125429
[7] Meyer W, Biedermann K, Gubo M, Hammer L and Heinz K 2008 *J. Phys.: Condens. Matter* **20** 304204
[8] Meyer W, Hock D, Biedermann K, Gubo M, Hammer L, Müller S and Heinz K 2008 *Phys. Rev. Lett.* **101** 016103
[9] Küppers J and Michel H 1979 *Appl. Surf. Sci.* **3** 179
[10] Heinz K, Schmidt G, Hammer L and Müller K 1985 *Phys. Rev.* B **32** 6214
[11] Lerch D, Klein A, Schmidt A, Müller S, Hammer L, Heinz K and Weinert M 2006 *Phys. Rev.* B **73** 075430
[12] Heinz K 1995 *Rep. Prog. Phys.* **58** 637
[13] Pendry J B 1980 *J. Phys. C: Solid State Phys.* C **13** 937
[14] Will G, Masciocchi N, Parrish W and Hart M 1987 *J. Appl. Chem.* **20** 394
[15] Ebensperger C, Gubo M, Meyer W, Hammer L and Heinz K 2009 in preparation
[16] Pejova B, Isahi A, Najdoski M and Grozdanov I 2001 *Mater. Res. Bull.* **36** 161
[17] Yamamoto H, Tanaka S and Hirao K 2004 *J. Ceram. Soc. Japan* **112** S876
[18] Shinde V R, Mahadik S B, Gujar T P and Lokhande C D 2006 *Appl. Surf. Sci.* **252** 7487
[19] Drasovean R, Monteiro R, Fortunato E and Musat V 2006 *J. Non-Cryst. Solids* **352** 1470
[20] Meyer W, Biedermann K, Gubo M, Hammer L and Heinz K 2009 *Phys. Rev.* B submitted
[21] Heinz K, Starke U and Bothe F 1991 *Surf. Sci.* **243** L70
[22] Torelli P, Soares E A, Renaud G, Valeri S, Guo X X and Luches P 2007 *Surf. Sci.* **601** 2651
[23] Wollschläger J, Erdös D and Schröder K M 1998 *Surf. Sci.* **402** 272
[24] Vassent J L, Dynna M, Marty A, Gilles B and Patrat G 1996 *J. Appl. Phys.* **80** 5727
[25] Dynna M, Vassent J L, Marty A and Gilles B 1996 *J. Appl. Phys.* **80** 2650
[26] Redman M J and Steward E G 1962 *Nature* **193** 867
[27] Risbud A S, Snedeker L P, Elcombe M M, Cheetham A K and Seshadari R 2005 *Chem. Mater.* **17** 834

[28] Noguera C 2000 *J. Phys.: Condens. Matter* **12** R367
[29] Goniakowski J, Finocchi F and Noguera C 2008 *Rep. Prog. Phys.* **71** 016501
[30] Han M J and Yu J 2006 *J. Korean Phys. Soc.* **48** 1496
[31] Wander A, Bush I J and Harrison N M 2003 *Phys. Rev.* B **68** 233405
[32] Mitchell D E and Heuer A W *Dislocations in Solids* vol 12, ed F R N Nabaroo and J P Hirth (Amsterdam: Elsevier)